

Identification of MHD compressible modes in interstellar plasma with synchrotron emission polarization

ALEXEY CHEPURNOV,¹ ALEX LAZARIAN,¹ REINALDO SANTOS DE LIMA,² AND SARAH APPLEBY³

¹*Department of Astronomy, University of Wisconsin, Madison, US*

²*University of São Paulo, Brazil*

³*Edinburgh University, UK*

ABSTRACT

We provide a procedure for identification of dominating compressible and Alfvénic MHD modes or isotropic turbulence in synchrotron emission polarization maps of Galactic objects. The results for the region of North Galactic Pole, Orion molecular cloud complex and the star-forming complex Cygnus X are presented.

Keywords: methods: data analysis — turbulence — ISM: magnetic fields — techniques: miscellaneous

1. INTRODUCTION

Turbulence is ubiquitous and plays crucial roles in various interstellar processes including star formation and dynamo and transport processes. Interstellar medium (ISM) is magnetized, indicating the magneto-hydrodynamic (MHD) nature of turbulence in ISM. As the result, it is theoretically expected that interstellar turbulence can have three MHD modes, Alfvén, fast and slow compressible modes (Cho & Lazarian 2003; Yan & Lazarian 2004). It is challenging to remotely diagnose the MHD modes of turbulence except for the nearby solar wind turbulence which can be directly detected by space probes, (Erdélyi et al. 2002). Here we report the detection of MHD modes of interstellar turbulence using Galactic synchrotron polarization data.

We developed a new technique based on polarization data of synchrotron emission which does not require estimation of power spectrum from observational data.

Turbulence anisotropy is imprinted in the set of Stokes parameters (I, Q, U), which characterize the polarization state of radiation. We use here the values (I+Q)/2 and U/2, whose emissivities are proportional to the squared picture-plane projection of the magnetic field, and the product of perpendicular picture plane projections respectively.

Their variances as functions of Stokes parameters positional angle (hereafter we name them "signatures") can be parametrized so that one of the parameters can be used to identify the dominating MHD mode.

2. MAGNETIC FIELD

Let us consider a model where the turbulent magnetic field is a homogeneous random field which can be described with its spectral representation (see Sect. G for the details):

$$B_i(\mathbf{r}) = \int \sqrt{d\mathbf{k}} e^{i\mathbf{k}\mathbf{r}} F(\mathbf{k}) T_{ij}(\hat{\mathbf{k}}) \xi_j(\mathbf{k}) \quad (1)$$

where the spectral tensor T and random field ξ conform the following rules: $T_{ij} = T_{il}T_{jl}$, $\langle \xi_i(\mathbf{k}) \xi_j^*(\mathbf{k}') \rangle = \delta_{ij} \delta_{\mathbf{k}\mathbf{k}'}$, $\xi_i(-\mathbf{k}) = \xi_i^*(\mathbf{k})$ and $F(\mathbf{k})$ is the square root of the scalar part of the power spectrum.

The terms forming the spectral representation are different for different modes. We assume here that the turbulent magnetic field has axial symmetry, defined by the mean magnetic field with the direction $\hat{\lambda}$, see Fig. 1.

Let us define magnetic field power spectra for different MHD modes, following Lazarian & Pogosyan (2012).

The spectral tensor of the axially-symmetrical magnetic field can be combined of the two parts, T_E and T_F :

$$T_{E,ij}(\hat{\mathbf{k}}) = \delta_{ij} - \hat{k}_i \hat{k}_j \quad (2)$$

$$T_{F,ij}(\hat{\mathbf{k}}) = \frac{(\hat{\mathbf{k}}\hat{\lambda})^2 \hat{k}_i \hat{k}_j + \hat{\lambda}_i \hat{\lambda}_j - (\hat{\mathbf{k}}\hat{\lambda})(\hat{k}_i \hat{\lambda}_j + \hat{\lambda}_i \hat{k}_j)}{1 - (\hat{\mathbf{k}}\hat{\lambda})^2} \quad (3)$$

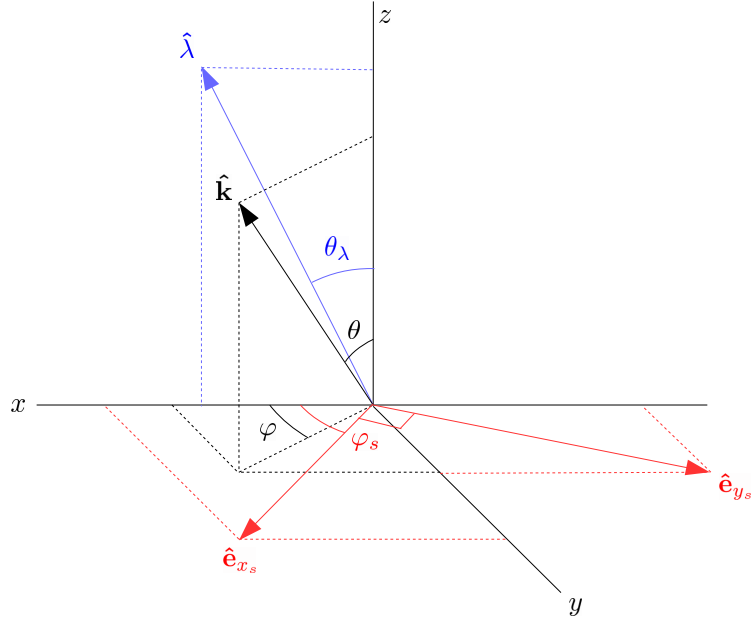


Figure 1. Vectors and angles involved in calculating of spectral tensor projections. $\hat{\lambda}$ is the symmetry axis, $\hat{\mathbf{k}}$ is the direction of the wavevector, vectors $\hat{\mathbf{e}}_{x_s}$ and $\hat{\mathbf{e}}_{y_s}$ define the frame of the Stokes parameters, the axis Oz points to the observer.

Then, the terms defining power spectra of the MHD modes are given below.

Alfvénic mode:

$$T_{ij}(\hat{\mathbf{k}}) = T_{E,ij}(\hat{\mathbf{k}}) - T_{F,ij}(\hat{\mathbf{k}}) \quad (4)$$

$$F_0^2(\hat{\mathbf{k}}) = \exp \left(-M_a^{-4/3} \frac{|\hat{\mathbf{k}}\hat{\lambda}|}{(1 - (\hat{\mathbf{k}}\hat{\lambda})^2)^{1/3}} \right) \quad (5)$$

Fast mode:

$$T_{ij}(\hat{\mathbf{k}}) = T_{F,ij}(\hat{\mathbf{k}}) \quad (6)$$

$$F_0^2(\hat{\mathbf{k}}) = \begin{cases} 1, & \beta \ll 1 \\ 1 - (\hat{\mathbf{k}}\hat{\lambda})^2, & \beta \gtrsim 1 \end{cases} \quad (7)$$

Slow mode (high- β only):

$$T_{ij}(\hat{\mathbf{k}}) = T_{F,ij}(\hat{\mathbf{k}}) \quad (8)$$

$$F_0^2(\hat{\mathbf{k}}) = \exp \left(-M_a^{-4/3} \frac{|\hat{\mathbf{k}}\hat{\lambda}|}{(1 - (\hat{\mathbf{k}}\hat{\lambda})^2)^{1/3}} \right) \quad (9)$$

here M_a is the Alfvénic Mach number and F_0^2 is the factor defining the anisotropy of the scalar part of the power spectrum F^2 :

$$F^2(\mathbf{k}) \propto \frac{e^{-(\frac{2\pi}{kL})^2}}{k^{11/3}} F_0^2(\hat{\mathbf{k}}) \quad (10)$$

where L is the injection scale.

We are interested in calculating of quantities related to Stokes parameters, which are expressed via magnetic field in the following way (omitting the scaling coefficient):

$$I(\mathbf{R}) = \int w(z) dz (B_{x_s}^2(\mathbf{r}) + B_{y_s}^2(\mathbf{r})) \quad (11)$$

$$Q(\mathbf{R}) = \int w(z) dz (B_{x_s}^2(\mathbf{r}) - B_{y_s}^2(\mathbf{r})) \quad (12)$$

$$U(\mathbf{R}) = \int w(z) dz 2B_{x_s}(\mathbf{r})B_{y_s}(\mathbf{r}) \quad (13)$$

here w is the window function defining the borders of the emitting structure. We assume here that the lines of sight corresponding to picture plane are parallel and the 2D vector \mathbf{R} gives us the coordinates in the picture plane. In some cases it is not completely true, but we assume that it is an acceptable approximation.

In this work we often use numerical evaluation of Eq. 1 to generate magnetic field for a particular MHD mode and calculate correspondent Stokes parameter maps by applying¹ Eqs. 11 - 13. Hereafter we name such data synthetic.

3. EMISSIVITY CORRELATION FUNCTIONS AND POWER SPECTRA

In this section we shall derive correlation functions and power spectra of emissivities related to MHD mode signatures.

3.1. The case of $(I+Q)/2$

The corresponding emissivity can be defined as follows:

$$\begin{aligned} \varepsilon_{xx}(\mathbf{r}) &= (B_{0\perp} \cos \varphi_s + B_i \hat{e}_{x_s i})^2 \\ &= B_{0\perp}^2 \cos^2 \varphi_s + 2B_{0\perp} \cos \varphi_s B_i \hat{e}_{x_s i} + (B_i \hat{e}_{x_s i})^2 \end{aligned} \quad (14)$$

where $B_{0\perp}$ is the picture-plane projection of mean magnetic field.

Using the spectral representation of turbulent magnetic field Eq. 1, we can write the following expression for the emissivity correlation function:

$$\begin{aligned} C_{xx}(\mathbf{r}) &\equiv \langle \varepsilon_{xx}(\mathbf{r}) \varepsilon_{xx}(\mathbf{0}) \rangle \\ &= \left\langle \left(B_{0\perp}^2 \cos^2 \varphi_s + 2B_{0\perp} \cos \varphi_s \int \sqrt{d\mathbf{k}_1} e^{i\mathbf{k}_1 \mathbf{r}} F(\mathbf{k}_1) \hat{e}_{x_s i_1} T_{i_1 j_1}(\hat{\mathbf{k}}_1) \xi_{j_1}(\mathbf{k}_1) \right. \right. \\ &\quad + \int \sqrt{d\mathbf{k}_2} e^{i\mathbf{k}_2 \mathbf{r}} F(\mathbf{k}_2) \hat{e}_{x_s i_2} T_{i_2 j_2}(\hat{\mathbf{k}}_2) \xi_{j_2}(\mathbf{k}_2) \\ &\quad \cdot \left. \int \sqrt{d\mathbf{k}_3} e^{i\mathbf{k}_3 \mathbf{r}} F(\mathbf{k}_3) \hat{e}_{x_s i_3} T_{i_3 j_3}(\hat{\mathbf{k}}_3) \xi_{j_3}(\mathbf{k}_3) \right) \\ &\quad \cdot \left(B_{0\perp}^2 \cos^2 \varphi_s + 2B_{0\perp} \cos \varphi_s \int \sqrt{d\mathbf{k}'_1} F(\mathbf{k}'_1) \hat{e}_{x_s i'_1} T_{i'_1 j'_1}(\hat{\mathbf{k}}'_1) \xi_{j'_1}(\mathbf{k}'_1) \right. \\ &\quad + \int \sqrt{d\mathbf{k}'_2} F(\mathbf{k}'_2) \hat{e}_{x_s i'_2} T_{i'_2 j'_2}(\hat{\mathbf{k}}'_2) \xi_{j'_2}(\mathbf{k}'_2) \\ &\quad \cdot \left. \left. \int \sqrt{d\mathbf{k}'_3} F(\mathbf{k}'_3) \hat{e}_{x_s i'_3} T_{i'_3 j'_3}(\hat{\mathbf{k}}'_3) \xi_{j'_3}(\mathbf{k}'_3) \right) \right) \rangle \end{aligned} \quad (15)$$

The combinations of wavevectors, giving non-zero contribution to Eq. 15, can be found accounting for Eqs. G35 and G33. The correspondent list is presented in Tab.1.

Evaluating averaging in Eq. 15 and accounting for Tab.1 and Eq. G28, we have:

$$\begin{aligned} C_{xx}(\mathbf{r}) &= (2B_{0\perp} \cos \varphi_s)^2 \int d\mathbf{k} F^2(\mathbf{k}) e^{i\mathbf{k} \mathbf{r}} \hat{e}_{x_s i} \hat{e}_{x_s j} T_{ij}(\hat{\mathbf{k}}) \\ &\quad + 2 \left(\int d\mathbf{k} F^2(\mathbf{k}) e^{i\mathbf{k} \mathbf{r}} \hat{e}_{x_s i} \hat{e}_{x_s j} T_{ij}(\hat{\mathbf{k}}) \right)^2 \end{aligned} \quad (16)$$

Then the correspondent power spectrum and its components can be written as follows:

$$F_{xx}^2(\mathbf{k}) = F_{xx,l}^2(\mathbf{k}) + F_{xx,q}^2(\mathbf{k}) \quad (17)$$

where

$$F_{xx,l}^2(\mathbf{k}) = (2B_{0\perp} \cos \varphi_s)^2 \mathcal{F}_{xx}^2(\mathbf{k}) \quad (18)$$

¹ With addition of a constant component of magnetic field.

Table 1. List of wavevector combinations, giving non-zero contribution to Eq. 15 (the correlation function of emissivity of $(I+Q)/2$).

combinations of ξ	combinations of \mathbf{k}	note
$\langle \xi_{j_1}(\mathbf{k}_1) \xi_{j'_1}(\mathbf{k}'_1) \rangle$	$\mathbf{k}_1 = -\mathbf{k}'_1$	
$\langle \xi_{j_2}(\mathbf{k}_2) \xi_{j'_2}(\mathbf{k}'_2) \xi_{j_3}(\mathbf{k}_3) \xi_{j'_3}(\mathbf{k}'_3) \rangle$	$\mathbf{k}_2 = -\mathbf{k}'_2$ & $\mathbf{k}_3 = -\mathbf{k}'_3$	
	$\mathbf{k}_2 = -\mathbf{k}'_3$ & $\mathbf{k}_3 = -\mathbf{k}'_2$	
	$\mathbf{k}_2 = -\mathbf{k}_3$ & $\mathbf{k}'_2 = -\mathbf{k}'_3$	const
$\langle \xi_{j_2}(\mathbf{k}_2) \xi_{j_3}(\mathbf{k}_3) \rangle$	$\mathbf{k}_2 = -\mathbf{k}_3$	const
$\langle \xi_{j'_2}(\mathbf{k}'_2) \xi_{j'_3}(\mathbf{k}'_3) \rangle$	$\mathbf{k}'_2 = -\mathbf{k}'_3$	const

NOTE— Combinations giving constant contribution will be omitted.

$$F_{xx,q}^2(\mathbf{k}) = 2 \int d\mathbf{k}' \mathcal{F}_{xx}^2(\mathbf{k}') \mathcal{F}_{xx}^2(\mathbf{k} - \mathbf{k}') \quad (19)$$

and

$$\mathcal{F}_{xx}^2(\mathbf{k}) = F^2(\mathbf{k}) \hat{e}_{xsi} \hat{e}_{xsj} T_{ij}(\hat{\mathbf{k}}) \quad (20)$$

Hereafter $F_{xx,l}^2$ and $F_{xx,q}^2$ will be referred as linear and quadratic terms of the emissivity power spectrum of $(I+Q)/2$.

3.2. The case of $U/2$

The corresponding emissivity can be defined as follows:

$$\begin{aligned} \varepsilon_{xy}(\mathbf{r}) &= (B_{0\perp} \cos \varphi_s + B_i \hat{e}_{xsi})(-B_{0\perp} \sin \varphi_s + B_i \hat{e}_{ysi}) \\ &= -B_{0\perp}^2 \cos \varphi_s \sin \varphi_s - B_{0\perp} \sin \varphi_s B_i \hat{e}_{xsi} + B_{0\perp} \cos \varphi_s B_i \hat{e}_{ysi} + B_i \hat{e}_{xsi} B_{i'} \hat{e}_{ysi'} \end{aligned} \quad (21)$$

In a similar way we can obtain the following expressions for its power spectrum and its components:

$$F_{xy}^2(\mathbf{k}) = F_{xy,l}^2(\mathbf{k}) + F_{xy,q}^2(\mathbf{k}) \quad (22)$$

where

$$F_{xy,l}^2(\mathbf{k}) = (B_{0\perp} \sin \varphi_s)^2 \mathcal{F}_{xx}^2(\mathbf{k}) - 2B_{0\perp}^2 \sin \varphi_s \cos \varphi_s \mathcal{F}_{xy}^2(\mathbf{k}) + (B_{0\perp} \cos \varphi_s)^2 \mathcal{F}_{yy}^2(\mathbf{k}) \quad (23)$$

$$F_{xy,q}^2(\mathbf{k}) = \int d\mathbf{k}' \mathcal{F}_{xx}^2(\mathbf{k}') \mathcal{F}_{yy}^2(\mathbf{k} - \mathbf{k}') + \int d\mathbf{k}' \mathcal{F}_{xy}^2(\mathbf{k}') \mathcal{F}_{xy}^2(\mathbf{k} - \mathbf{k}') \quad (24)$$

and

$$\mathcal{F}_{xx}^2(\mathbf{k}) = F^2(\mathbf{k}) \hat{e}_{xsi} \hat{e}_{xsj} T_{ij}(\hat{\mathbf{k}}) \quad (25)$$

$$\mathcal{F}_{xy}^2(\mathbf{k}) = F^2(\mathbf{k}) \hat{e}_{xsi} \hat{e}_{ysj} T_{ij}(\hat{\mathbf{k}}) \quad (26)$$

$$\mathcal{F}_{yy}^2(\mathbf{k}) = F^2(\mathbf{k}) \hat{e}_{ysi} \hat{e}_{ysj} T_{ij}(\hat{\mathbf{k}}) \quad (27)$$

Here $F_{xy,l}^2$ and $F_{xy,q}^2$ are linear and quadratic terms of the emissivity power spectrum of $U/2$.

4. THE MODE SIGNATURE

If the emissivity has 3D power spectrum $F^2(\mathbf{k})$ and it is projected as described in Sect. 2, the correspondent picture plane power spectrum can be written as follows:

$$\Phi^2(\mathbf{K}) = (2\pi)^2 \int_{-\infty}^{\infty} |\tilde{w}(k_z)|^2 F^2(\mathbf{k}) dk_z \quad (28)$$

where $\mathbf{K} \equiv (k_x, k_y)$ and \tilde{w} is the Fourier-transformed window function.

Then we can write the following expression for related signature:

$$\begin{aligned} s(\varphi_s) &= \int d\mathbf{K} \Phi^2(\mathbf{K}) f^2(K) \\ &= \int w_{fz}(\mathbf{k}) d\mathbf{k} F^2(\mathbf{k}) \end{aligned} \quad (29)$$

where $f^2(K)$ is the filter which includes the beam smoothing and high-pass filter for improving statistics² with the filtering scale L_f . The spectral window function w_{fz} is defined as follows:

$$w_{fz}(\mathbf{k}) = (2\pi)^2 |\tilde{w}(k_z)|^2 f^2(K) \quad (30)$$

According to Eqs. 17 and 22, "theoretical" signatures consist of linear and quadratic terms³. The linear term is important because we expect it to dominate in the signal. It is also important that we can obtain analytic results in this case. We shall consider it in the next section.

4.1. Signature linear term

To calculate the signatures s_{xx} and s_{xy} we have to substitute Eq. 18 and Eq. 23 to Eq. 29:

$$s_{xx}(\varphi_s) = (2 \cos \varphi_s)^2 \int w_{fz}(\mathbf{k}) d\mathbf{k} F^2(\mathbf{k}) T_{xx}(\hat{\mathbf{k}}) \quad (31)$$

$$s_{xy}(\varphi_s) = \int w_{fz}(\mathbf{k}) d\mathbf{k} F^2(\mathbf{k}) \left(\sin^2 \varphi_s T_{xx}(\hat{\mathbf{k}}) - 2 \sin \varphi_s \cos \varphi_s T_{xy}(\hat{\mathbf{k}}) + \cos^2 \varphi_s T_{yy}(\hat{\mathbf{k}}) \right) \quad (32)$$

where

$$T_{xx}(\hat{\mathbf{k}}) = \hat{e}_{xsi} \hat{e}_{xsj} T_{ij}(\hat{\mathbf{k}}) \quad (33)$$

$$T_{xy}(\hat{\mathbf{k}}) = \hat{e}_{xsi} \hat{e}_{ysj} T_{ij}(\hat{\mathbf{k}}) \quad (34)$$

$$T_{yy}(\hat{\mathbf{k}}) = \hat{e}_{ysi} \hat{e}_{ysj} T_{ij}(\hat{\mathbf{k}}) \quad (35)$$

If we use here the spectral tensors T_E and T_F , we can reduce the signature expressions to the following forms:

$$s_{xx}(\varphi_s) = (a_{xx} \sin^2 \varphi_s + b_{xx}) \cos^2 \varphi_s \quad (36)$$

$$s_{xy}(\varphi_s) = a_{xy} \cos 4\varphi_s + b_{xy} \quad (37)$$

where the signature parameters a and b can be written as follows:

$$a_{xx}^E = \int w_{fz}(\mathbf{k}) d\mathbf{k} F^2(\mathbf{k}) (4 \cos 2\phi \sin^2 \theta) \quad (38)$$

$$b_{xx}^E = \int w_{fz}(\mathbf{k}) d\mathbf{k} F^2(\mathbf{k}) (3 + \cos 2\theta - 2 \cos 2\phi \sin^2 \theta) \quad (39)$$

$$a_{xx}^F = - \int w_{fz}(\mathbf{k}) d\mathbf{k} F^2(\mathbf{k}) \cdot \frac{4(\cos 2\phi \sin^2 \theta (\cos \theta \cos \theta_\lambda + \cos \phi \sin \theta \sin \theta_\lambda)^2 + \sin \theta_\lambda (\sin \theta_\lambda - \cos \phi (\cos \theta_\lambda \sin 2\theta + 2 \cos \phi \sin^2 \theta \sin \theta_\lambda)))}{1 - (\cos \theta \cos \theta_\lambda + \cos \phi \sin \theta \sin \theta_\lambda)^2} \quad (40)$$

$$b_{xx}^F = \int w_{fz}(\mathbf{k}) d\mathbf{k} F^2(\mathbf{k}) \cdot \frac{(2 \cos \phi \cos \theta_\lambda \sin 2\theta + (-3 + \cos 2\phi - 2 \cos^2 \phi \cos 2\theta) \sin \theta_\lambda)^2}{4(1 - (\cos \theta \cos \theta_\lambda + \cos \phi \sin \theta \sin \theta_\lambda)^2)} \quad (41)$$

The corresponding signature parameters for the Alfvénic mode are

$$\begin{aligned} a^{alf} &= a^E - a^F \\ b^{alf} &= b^E - b^F \end{aligned} \quad (42)$$

² This filter is also used for mode identification, see below.

³ For observed signatures odd powers of turbulent magnetic field are relevant too, because ensemble averaging is not possible in this case (see Sect. 4.2).

For fast and slow modes they are

$$\begin{aligned} a^{comp} &= a^F \\ b^{comp} &= b^F \end{aligned} \quad (43)$$

with proper $F^2(\mathbf{k})$ (see Sect. 2).

It is remarkable that the following relations between the parameters of xx - and xy -signatures

$$a_{xy} = \frac{1}{8}a_{xx} \quad (44)$$

$$b_{xy} = \frac{1}{8}(a_{xx} + 2b_{xx}) \quad (45)$$

do not depend on the mode type.

4.2. Impact of terms corresponding to odd powers of magnetic field

The direct expression for the signature s_{xx} through magnetic field is as follows:

$$s_{xx} = \frac{1}{\Omega} \int_{\Omega} d\mathbf{R} \left(\int d\mathbf{R}' (\delta(\mathbf{R}' - \mathbf{R}) - f(\mathbf{R}' - \mathbf{R})) \int dz' w(z') B_x^2(\mathbf{r}') \right)^2 \quad (46)$$

where \mathbf{R} is the picture-plane projection of \mathbf{r} , z is the coordinate over the line of sight, Ω is the map spot for signature calculation and $B_x = B_{0x} + B_{x,turb}$.

As we can see here, some of the terms corresponding to odd powers of turbulent magnetic field do not diminish as we do not do ensemble averaging here.

The terms corresponding to $B_{0x}^3 B_{x,turb}(\mathbf{r}'')$ and $B_{0x} B_{x,turb}^3(\mathbf{r}'')$ are zero, because the operator $\int d\mathbf{R}' (\delta(\mathbf{R}' - \mathbf{R}) - f(\mathbf{R}' - \mathbf{R}))$ gives zero when applied to a constant⁴.

So, the only odd-power term giving non-zero contribution corresponds to $B_{0x} B_{x,turb}(\mathbf{r}') B_{x,turb}^2(\mathbf{r}'')$. Using the spectral representation for $B_{x,turb}$ after some algebra we can write out the following expression for its variance:

$$\begin{aligned} \langle s_{xx,odd}^2 \rangle &= 16B_{0x}^2 (2\pi)^9 \int d\mathbf{k}_1 F^2(\mathbf{k}_1) \int d\mathbf{k}_2 F^2(\mathbf{k}_2) \int d\mathbf{k}_3 F^2(\mathbf{k}_3) \cdot (\\ &4(j^2(|\mathbf{K}_2| R_0) + j^2(|\mathbf{K}_1 + \mathbf{K}_2 + \mathbf{K}_3| R_0)) \tilde{w}(\mathbf{k}_1 + \mathbf{k}_2) \tilde{w}(\mathbf{k}_1) \tilde{w}(\mathbf{k}_2 + \mathbf{k}_3) \tilde{w}(\mathbf{k}_3) \\ &+ 2j^2(|\mathbf{K}_1 + \mathbf{K}_2 + \mathbf{K}_3| R_0) \tilde{w}^2(\mathbf{k}_1 + \mathbf{k}_2) \tilde{w}^2(\mathbf{k}_3)) \end{aligned} \quad (47)$$

where F^2 is the power spectrum of $B_{x,turb}$, $j(x) \equiv J_1(x)/x$, R_0 is a spot radius and \tilde{w} is a Fourier transform of

$$w(\mathbf{r}) \equiv (\delta(\mathbf{R}) - f(\mathbf{R})) \cdot w(z) \quad (48)$$

We also assume here that $w(\mathbf{r})$ is an even function.

Calculations using synthetic data show, that this term can be of the same order of magnitude as the quadratic one, being of unpredictable shape. This makes the investigation of quadratic term's behavior unneeded. We shall further assume that the linear term is dominating over these two ones. This assumption will be also checked using synthetic data.

4.3. Fourier decomposition

As we can see from Eqs. 36 and 37, the linear term signatures have limited spectrum: only three first Fourier harmonics are non-zero (in addition, for the xy -signature the second harmonic is zero too). As practice shows, this is true for any signature, including quadratic and odd-power terms and real signatures obtained from observational data.

So we can state the following for the signature Fourier coefficients:

$$f_{xy,s,n}^{xx,c} \equiv \frac{2}{\pi} \int_0^\pi s_{xy}^{xx}(\varphi_s) \cos(2n\varphi_s) d\varphi_s \quad (49)$$

$$f_{*,*,n} = 0, n > 2 \quad (50)$$

⁴ Variable \mathbf{r}'' appears when expanding square in Eq. 46

$$f_{xy,*,1} = 0 \quad (51)$$

In addition, the rules Eqs. 44 and 45 can be mapped to Fourier space as follows:

$$f_{xy,c,2} = -f_{xx,c,2} \quad (52)$$

$$f_{xy,c,0} = \frac{1}{2}f_{xx,c,0} - f_{xx,c,2} \quad (53)$$

Numerical calculations show, that these rules apply to quadratic and odd-power terms too.

For signatures obtained from observational data Eq. 52 holds with very high accuracy, while the disparity of Eq. 53 is larger, being still small. Additionally, for non-symmetrical signatures we have the following rule:

$$f_{xy,s,2} = -f_{xx,s,2} \quad (54)$$

which holds with very high accuracy, like Eq. 52.

5. IDENTIFICATION OF MHD MODES

Let us introduce the parameter which is further used for MHD modes identification:

$$r_{xx} \equiv \frac{a_{xx}}{b_{xx}} \quad (55)$$

We also need its derivative over filtering scale L_f of our high-pass filter for this purpose (see Eq. 29).

It is important that the line of sight window function $w(z)$, contributing to Eq. 30 is not constant, because otherwise $\tilde{w} \sim \delta(k_z)$ and dependence on K in Eqs. 38, 39, 40, 41 factorizes and cancels in Eq. 55, what means that r_{xx} does not depend on L_f in this case.

Another reason not to take such simplification is because we can reproduce observed positive r_{xx} only in the case of small enough line-of-sight extent of an emitting structure with Alfvénic mode.

In order to determine the classification rule we do a parameter space study within their expected parameter ranges, by numerical evaluation of Eqs. 42 and 43.

The results of parameter space scanning are presented in Tab. 2. The parameter ranges are: $M_a \in [0.1, 0.9]$, $\theta_\lambda \in [10^\circ, 80^\circ]$, $L_z \in [0.5, 2]$, $L_f \in [0.25, 4]$, $L = 1$.

Table 2. Fraction of negative parameters for linear term (direct calculation)

MHD mode	$\partial r_{xx}/\partial L_f$	r_{xx}
Alfvénic	0.00 %	69.33 %
slow	79.73 %	100.00 %
fast, high β	65.33 %	100.00 %
fast, low β	34.67 %	100.00 %

We can see, that the sign of the trend $\partial r_{xx}/\partial L_f$ is always positive for Alfvénic mode and can be negative only for compressible modes.

The sign of r_{xx} can be positive only for the Alfvénic mode, and the negative sign of r_{xx} is possible for both compressible and Alfvénic modes.

This behavior allows us to identify dominating compressible and Alfvénic modes using parameter signs as shown on Fig. 2.

However, in reality we cannot separate the linear term and so we need to account for other signal components such as quadratic or odd-power terms, what can be done using synthetic data.

The results of parameter space scanning for this total signal are presented in Tab. 3. The parameter ranges are: $M_a \in [0.1, 0.7]$, $\theta_\lambda \in [20^\circ, 80^\circ]$, $L_f \in [0.25, 3]$, $L_z = L = 1$.

As we can see, in general our identification recipe stays valid, if we can admit a small number of false detections of compressible modes.

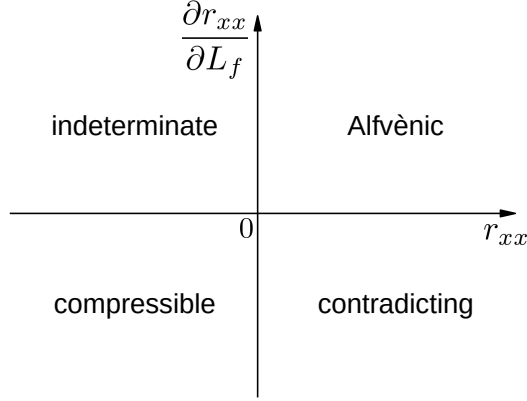


Figure 2. MHD mode classification rule with respect to signs of parameters $\partial r_{xx}/\partial L_f$ and r_{xx} .

Table 3. Fraction of negative parameters for total signal (synthetic data)

MHD mode	$\partial r_{xx}/\partial L_f$	r_{xx}
Alfvénic	5.56 %	88.69 %
slow	79.86 %	100.00 %
fast, high β	62.50 %	100.00 %
fast, low β	40.97 %	100.00 %

6. DATA PROCESSING

The observed signatures and related values of r_{xx} and $\Delta r_{xx}/\Delta L_f$ are calculated as follows. We select the data inside a region with given radius and intensity level range. Then we rotate the Stokes parameters frame to the direction of mean magnetic field, what is equivalent to making the mean Q parameter maximal. After that we apply our high-pass filter to the I, Q, U maps, what is needed for improving statistics and for further classification. Then we calculate the variances of $(I+Q)/2$ and $U/2$ gradually rotating the frame of the Stokes parameters by given $\Delta\varphi_s$. Obtained dependencies of the variances of $(I+Q)/2$ and $U/2$ on rotation angle φ_s form the signatures \hat{s}_{xx} and \hat{s}_{xy} .

If the relative variance of \hat{s}_{xx} is small enough, we can guess that the signal is caused by the quadratic term of an isotropic field, so the signature is classified as "isotropic". If it is not the case, we try to figure out if the model of axially-symmetrical magnetic field statistics can be applied.

The sine coefficients for the theoretical signatures are zero, because they are symmetric, but for the observed ones it is not true. In this case their magnitude relative to constant term (asymmetry) can be used for estimating applicability of axially-symmetric magnetic field model. For the asymmetry threshold we take the relative deviation of the signal due to statistical fluctuations, which can be estimated from the magnetic field power spectrum and filter parameters, as described in Sect. F.

To recover the parameter r_{xx} we remove the constant component equal to $\hat{s}_{xx}(90^\circ)$ from the xx -signature and the related value from the xy one (using Eq. 45) and fit the linear term theoretical signatures by the technique of least squares⁵. Then the procedure is repeated for different value of L_f to calculate the trend $\Delta r_{xx}/\Delta L_f$ needed for the mode identification.

6.1. Data processing validation and compressible mode observability

⁵ Non-zero value of $\hat{s}_{xx}(90^\circ)$ can be caused by the contribution of quadratic and odd-power terms only. We also apply a threshold to this value to make sure that this impact is marginal.

The detection maps corresponding to synthetic magnetic field for particular MHD modes are presented on Fig. 3. This simulation shows, that our mode identification procedure stays valid regardless of presence of contamination related to higher order terms.

However, we must admit that we are not able to identify a MHD mode in every point of the map. This is the side effect of our identification procedure, which can be applied to spots with symmetric enough signatures only.

The identification patterns typical to these three simulated maps can be found on the real map of the North Galactic Pole region, see Fig. 5.

An important question is if we can detect compressible modes at all, taking into account that Alfvénic mode can dominate.

If we plot mode signal magnitude as function of θ_λ for different MHD modes (see Fig. 4), we can see that at 90° Alfvénic signal is zero while slow and fast ones have their maximum. So Alfvénic signal can be suppressed with respect to compressible ones even if the corresponding field is stronger, what can explain observability of compressible modes.

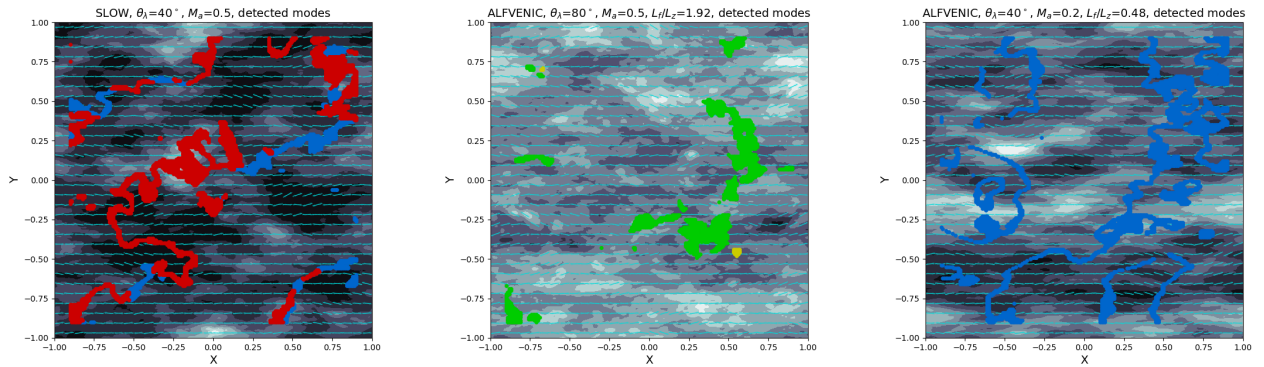


Figure 3. Mode detection for Stokes parameter maps obtained from synthetic magnetic field (total signal). Left map corresponds to slow MHD mode, the compressible one. Middle map corresponds to Alfvénic mode with $L_f > L_z$, $r_{xx} > 0$. Right map corresponds to Alfvénic mode with $L_f < L_z$, $r_{xx} < 0$. Red marks designate spots, classified as "compressible", green marks are "Alfvénic", yellow ones are "contradicting" and blue ones are "indeterminate".

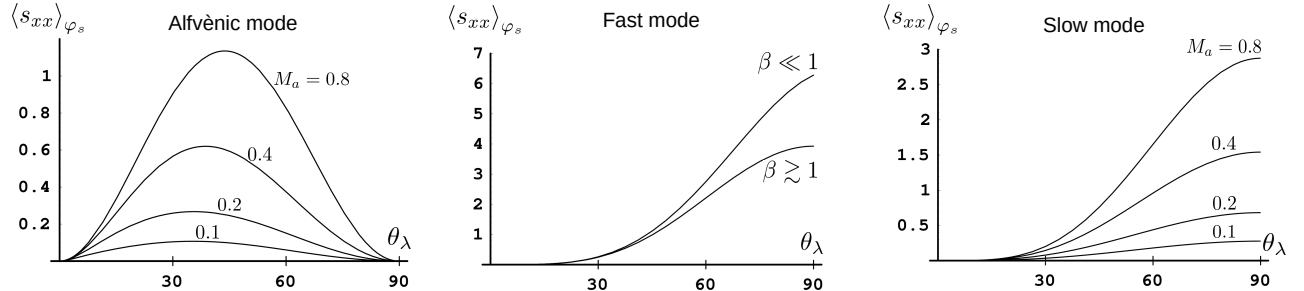


Figure 4. Signal magnitude as function of θ_λ for different MHD modes.

7. RESULTS OF OBSERVATIONAL DATA PROCESSING

In this work we investigate the presence of compressible MHD modes in the turbulent interstellar medium using polarization maps of radio-frequency synchrotron emission. We study three Galactic regions of the ISM: the vicinity of the North Galactic Pole (NGP), the Orion molecular cloud complex and the star-forming complex Cygnus X. We use the DRAO 1.4 GHz polarization survey with angular resolution $36'$ (Wolleben et al. 2006) for the NGP region and Orion complex, and employ Urumqi 6cm polarization survey with resolution $9'$ (Xiao et al. 2011) for Cygnus X complex, see Figures 5, 6 and 7.

All three regions display presence of compressible MHD modes. The presence of "contradicting" data is quite small, what also confirms validity of our technique.

Faraday rotation for NGP map spots with detected modes is $10^\circ \div 15^\circ$, and regarding Sect. D has marginal influence⁶.

The dominance of compressible turbulence in star-forming regions is consistent with the picture of turbulence injection by the highly supersonic flows (inside the dense and cold molecular clouds), generated by supernova explosions and outflows of YSOs.

Another option for observing a compressible signal could be suppressing the Alfvénic signal with respect to compressible ones due to a small angle between mean magnetic field and picture plane, as shown in Sect. 6.1. This could be the case for detection of a compressible mode in the NGP region.

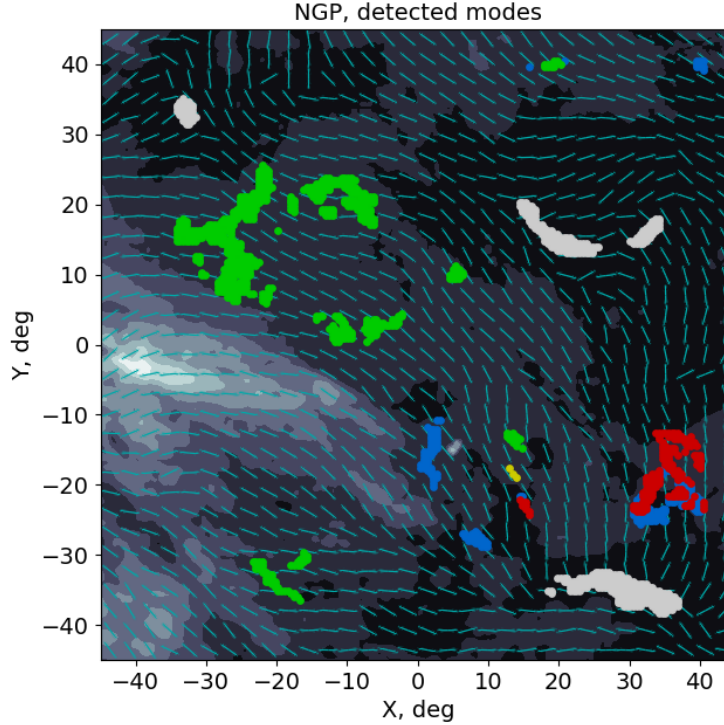


Figure 5. Detected modes of turbulence in the vicinity of the North Galactic Pole. Green dots designate spots with domination of Alfvénic mode, red ones designate domination of compressible modes and white dots correspond to isotropic turbulence. Blue dots correspond to spots with indeterminate status, yellow dots represent data contradicting our analysis. Spot radius is $9^\circ.5$ or 80 pc.

⁶ This Faraday rotation is estimated from all-sky Faraday rotation map by [Oppermann et al. \(2015\)](#).

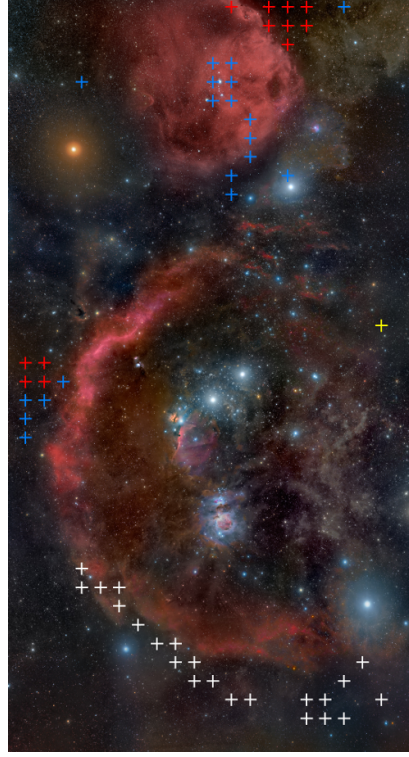


Figure 6. Detected modes of turbulence in the Orion molecular cloud complex. Red crosses designate domination of the compressible modes and white crosses correspond to the isotropic turbulence. Blue crosses correspond to spots with indeterminate status, yellow crosses represent contradicting data. Spot radius is $6''.4$ or 50 pc, map size is $14^\circ \times 24^\circ$.

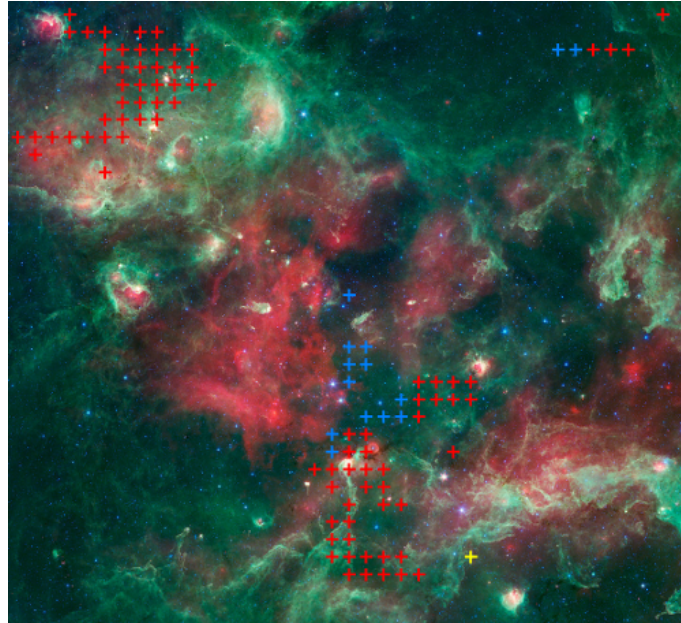


Figure 7. Detected modes of turbulence in Cygnus X star formation region. Red crosses designate domination of the compressible modes, blue crosses correspond to spots with indeterminate status, yellow crosses represent contradicting data. Spot radius is $1''.05$ or 26 pc, map size is $5^\circ \times 5^\circ$.

8. ASSUMPTIONS SUMMARY

We use the following assumptions for our technique.

- Lines of sight within the observed structure can be considered parallel. For the objects Orion and Cygnus X it is true. For the NGP region this approximation still can be used, because only anisotropy effects are relevant for us, while convergence of lines of sight is responsible for change of scales only.
- Faraday rotation influence can be considered marginal. For the case of NGP region the observed values of Faraday rotation do not affect our result, as estimated in Sect. D. For Orion and Cygnus X objects Faraday rotation within the object is unknown.
- The relativistic electron spectral index $\gamma = 5$ is assumed in calculation of Stokes parameters. As shown in Lazarian & Pogosyan (2012), the change of the index does not change the spatial properties of correlations. It is also numerically checked in Sect. C, showing that deviation of γ from 5 does not affect our results.
- Scanning contamination does not change our results. As shown in Sect. B, it does not increase the number of false detections.
- Axially symmetric magnetic field model can be applicable. This axially symmetric model of MHD turbulence is suggested in Lazarian & Pogosyan (2012) on the basis of earlier theoretical and numerical work. The limitations of the model come from the variations of the magnetic field direction along the line of sight. In this work we check for applicability of this model by checking the symmetry of obtained signatures. As shown in Sect. 6.1 this data selection does not affect the validity of our results. The influence of symmetry axis variation on r_{xx} is also discussed in Sect. E.
- Results obtained for linear term are applicable for total signal. This assumption is proved numerically in Sect. 6.1 and Sect. A, with exception of a small number ($\sim 6\%$) of compressible mode false detections due to statistical effects.
- Compressible signal can dominate. Alfvénic linear term signal can be suppressed with respect to compressible ones for $\theta_\lambda \sim 90^\circ$, as shown in Sect. 6.1. However the Alfvénic quadratic term is not suppressed in this case, but it has much lower magnitude and a different shape with a maximum at $\varphi_s = 90^\circ$, what allows us to roughly subtract it together with the odd-power signal (see Sect. 6 for details).

APPENDIX

A. VERIFICATION WITH SYNTHETIC DATA

We have performed the comparison of directly calculated r_{xx} using Eqs. 42, 43 and 55, with the ones recovered from the synthetic data.

This way we can check both our analytic results for r_{xx} and the data processing procedure. The comparison shows good correspondence including the case when non-linear terms have been taken into account, see Tab. 4.

Table 4. Comparison of the directly calculated parameter r_{xx} , with the one recovered from synthetic data for different MHD modes

MHD mode	r_{xx} , direct calculation	r_{xx} , synthetic	r_{xx} , synthetic
	linear term	linear term	total signal
Alfvénic	-0.258	-0.240	-0.274
slow	-0.959	-0.958	-0.958
fast, low β	-0.429	-0.419	-0.415
fast, high β	-0.707	-0.701	-0.698

NOTE—The model parameters are as follows: $M_a = 0.25$, $\theta_\lambda = 70^\circ$, $L = L_z = 1$, $L_f = 2$, $L_b = 0.2$ (the latter is the beam scale).

B. THE IMPACT OF THE SCANNING CONTAMINATION

Most of present polarization data suffer from contamination in intensity channel, which is caused by errors when assembling the map from individual scans. Practice shows, that polarization angle is more reliable parameter than intensity in this case.

If we assume that polarization angle is not contaminated, we can adopt the model when the observed Stokes parameter is a product of an uncontaminated one and the common positive contamination factor α :

$$\begin{aligned}\hat{I} &= \alpha I \\ \hat{U} &= \alpha U \\ \hat{Q} &= \alpha Q\end{aligned}\tag{B1}$$

Then for the signal $S \equiv (I + Q)/2$ we have the same relation:

$$\hat{S} = \alpha S\tag{B2}$$

Let us write out the correspondent variance:

$$D\hat{S} = \int d\mathbf{K} (\tilde{\alpha}^2 \star F_s^2) \tilde{f}^2 = \int d\mathbf{K} F_s^2 (\tilde{\alpha}^2 \star \tilde{f}^2)\tag{B3}$$

where tilde denotes Fourier transform, f is our high-pass filter and F_s^2 is the signal emissivity power spectrum. Therefore the expression

$$\tilde{f}_\alpha^2 = \tilde{\alpha}^2 \star \tilde{f}^2\tag{B4}$$

gives us the modified filter. Let us model the scanning contamination factor as follows:

$$\alpha = 1 + \sqrt{2}\delta\alpha \cos \mathbf{K}_\Delta \mathbf{R}\tag{B5}$$

Then, the correspondent squared Fourier transform is as follows:

$$\tilde{\alpha}^2 \sim \delta(\mathbf{K}) + \frac{\delta\alpha}{2}(\delta(\mathbf{K} - \mathbf{K}_\Delta) + \delta(\mathbf{K} + \mathbf{K}_\Delta)) \quad (\text{B6})$$

which gives us the variance:

$$D\hat{S} \sim \int d\mathbf{K} F_s^2 \cdot \tilde{f}^2 + \frac{\delta\alpha}{2} \int d\mathbf{K} F_s^2 \cdot (\tilde{f}^2(\mathbf{K} - \mathbf{K}_\Delta) + \tilde{f}^2(\mathbf{K} + \mathbf{K}_\Delta)) \quad (\text{B7})$$

where the first term gives us the unchanged signature and the second one is the signature part affected by contamination.

While the filter term in the contaminated signature is non-zero at low frequencies, the contaminated signature is more affected by the statistical noise, what makes the calculated r_{xx} less reliable.

Another contaminating factor is the constant component, modulated by scanning. It produces the false signal with $r_{xx} = -1$ (this value does not depend on any parameters).

To estimate impact of these factors we have performed calculations using synthetic data.

The results of exploring of parameter space are presented in Tables 5 and 6. The parameter ranges are: $M_a \in [0.1, 0.7]$, $\theta_\lambda \in [20^\circ, 80^\circ]$, $L_f \in [0.25, 3]$, $L_z = L = 1$.

Table 5. Fraction of negative $\partial r_{xx}/\partial L_f$ for contaminated total signal

MHD mode	cont. level 5 %	cont. level 10 %	cont. level 20 %
Alfvénic	4.17 %	3.47 %	2.78 %
slow	31.94 %	10.42 %	0.00 %
fast, high β	25.69 %	6.94 %	0.00 %
fast, low β	15.97 %	4.17 %	0.00 %

Table 6. Fraction of negative r_{xx} for contaminated total signal

MHD mode	cont. level 5 %	cont. level 10 %	cont. level 20 %
Alfvénic	96.43 %	99.40 %	100.00 %
slow	100.00 %	100.00 %	100.00 %
fast, high β	100.00 %	100.00 %	100.00 %
fast, low β	100.00 %	100.00 %	100.00 %

As we can see here, scanning contamination does not increase the number of compressible mode false detections. However it decreases the chances to identify compressible and Alfvénic modes (cf. Tab. 3).

C. STOKES PARAMETERS FOR DIFFERENT SLOPE OF ELECTRON ENERGY SPECTRUM

Expressions for Stokes parameters Eqs. 11 - 13 are written for the case of relativistic electron spectral index γ equal to 5. Let us consider the different case.

For arbitrary γ the emissivities of Stokes parameters are as follows:

$$\begin{aligned} \varepsilon_{0,Q} &= |B_\perp|^a \\ \varepsilon_{0,U} &= 0 \end{aligned} \quad (\text{C8})$$

where $a = (\gamma - 1)/2$ and the transverse magnetic field component is aligned over x-axis of the Stokes parameter frame (see Pandya et al. (2016)).

Let us rotate the Stokes frame by angle φ :

$$\begin{aligned}\varepsilon_Q &= |B_\perp|^a \cos 2\varphi = B_\perp^2 (\cos^2 \varphi - \sin^2 \varphi) \cdot |B_\perp|^{a-2} \\ \varepsilon_U &= |B_\perp|^a \sin 2\varphi = 2B_\perp^2 \cos \varphi \sin \varphi \cdot |B_\perp|^{a-2}\end{aligned}\tag{C9}$$

And, finally:

$$\begin{aligned}\varepsilon_Q &= (B_x^2 - B_y^2) \cdot |B_\perp|^{a-2} \\ \varepsilon_U &= 2B_x B_y \cdot |B_\perp|^{a-2}\end{aligned}\tag{C10}$$

where (x, y) is the rotated coordinate system.

For the estimation of γ -dependence of the parameters r_{xx} and $\partial r_{xx}/\partial L_f$ we calculated Stokes parameters from synthetic magnetic field using Eq. C10. These simulations show, that for $\gamma \in [3.5, 6.5]$ parameters r_{xx} and $\partial r_{xx}/\partial L_f$ do not change their sign, so our identification recipe stays valid in this range, see Fig. 8.

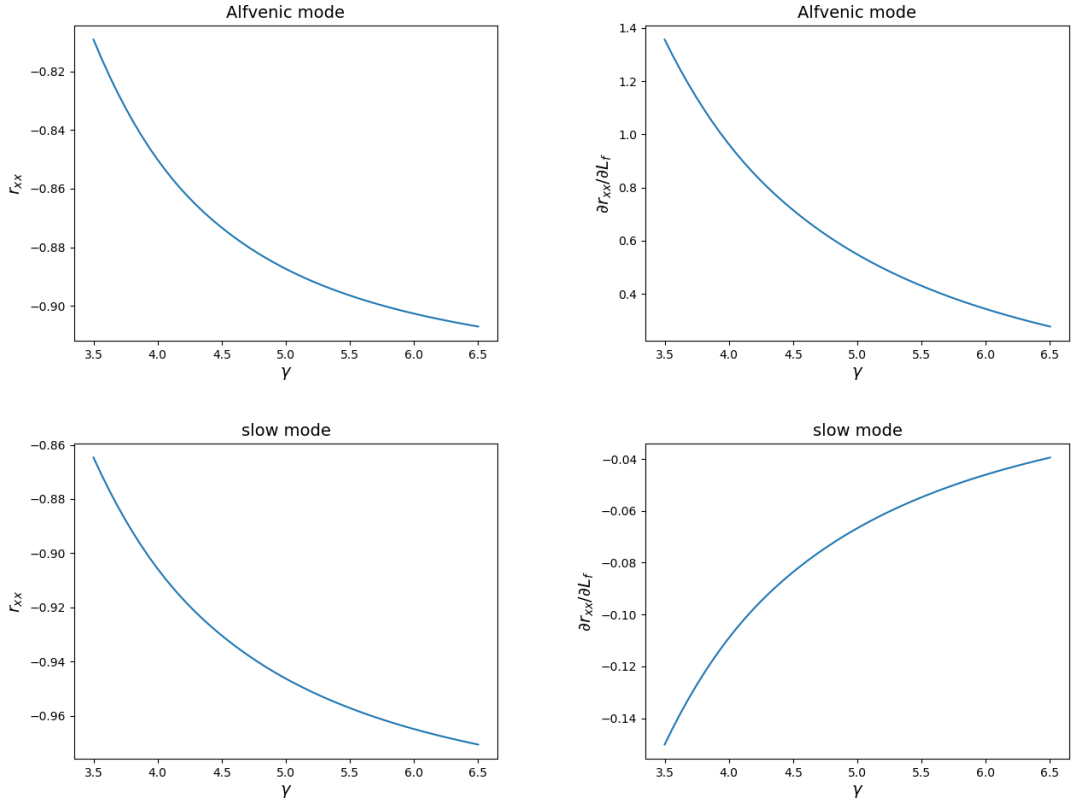


Figure 8. Example dependency of parameters r_{xx} (left) and $\partial r_{xx}/\partial L_f$ (right) for Alfvénic (top) and slow (bottom) modes on relativistic electron spectral index γ . Other calculation parameters are $M_a = 0.2$, $\theta_\lambda = 40^\circ$, $L_f/L_z = 0.36$.

D. ESTIMATION OF THE FARADAY ROTATION IMPACT

For the estimation of the Faraday rotation impact we calculated Stokes parameters (Eqs. 11, 12 and 13) from synthetic magnetic field, applying Faraday rotation numerically. Then the obtained maps were used to calculate the related parameters r_{xx} and $\partial r_{xx}/\partial L_f$.

These simulations show, that for Faraday rotation up to $\sim 30^\circ$ these parameters do not change their sign, so our identification recipe stays valid in this range, see Fig. 9.

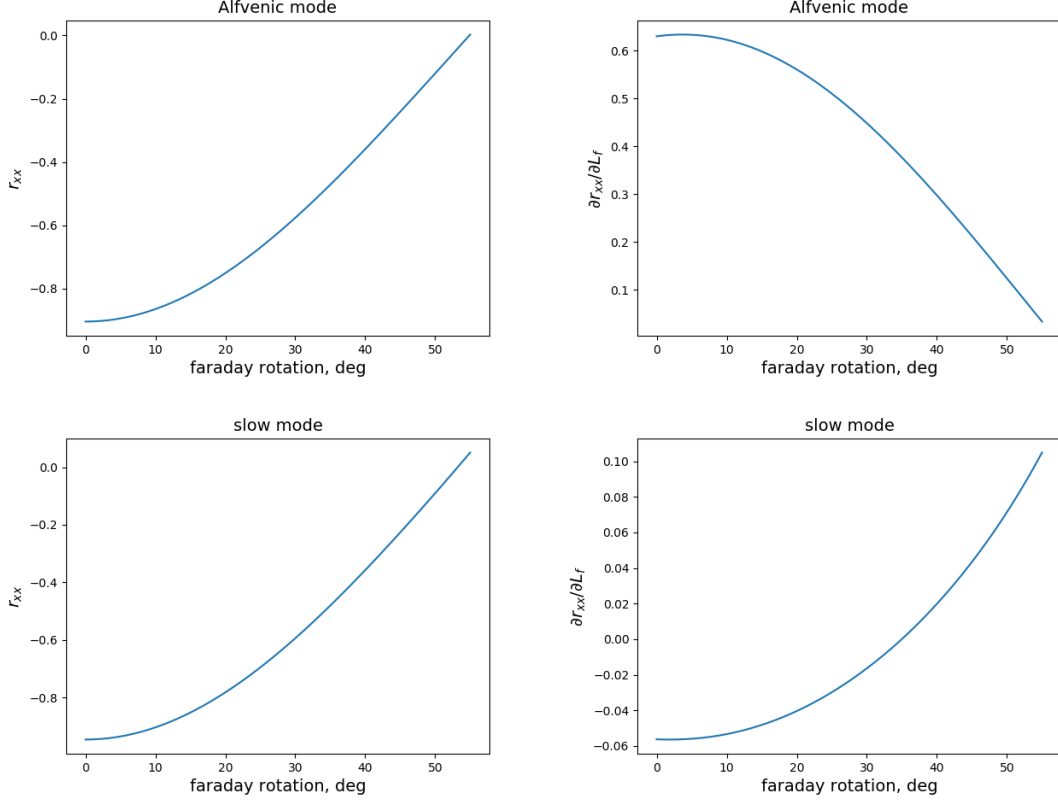


Figure 9. Example of Faraday rotation impact on parameters r_{xx} (left) and $\partial r_{xx} / \partial L_f$ (right) for Alfvénic (top) and slow (bottom) modes. Other calculation parameters are $M_a = 0.2$, $\theta_\lambda = 40^\circ$, $L_f / L_z = 0.36$.

E. ACCOUNTING FOR FLUCTUATIONS OF THE SYMMETRY AXIS

Let us model the influence of the symmetry axis fluctuations on the signature linear term as follows:

$$s_{xx}^{fluct}(\varphi_s) = \frac{1}{2\Delta\varphi_s} \int_{-\Delta\varphi_s}^{\Delta\varphi_s} s_{xx}(\varphi_s - \varphi'_s) d\varphi'_s \quad (\text{E11})$$

where $\Delta\varphi_s$ is the fluctuation angle.

After such operation the signature value at 90° is not zero any more:

$$s_{xx}^{fluct}(90^\circ) = \frac{1}{32\Delta\varphi_s} (4(a_{xx} + 4b_{xx})\Delta\varphi_s - 8b_{xx} \sin 2\Delta\varphi_s - a_{xx} \sin 4\Delta\varphi_s) \quad (\text{E12})$$

If we subtract this value from Eq. (E11), we have the signature of the form Eq. (36) with the parameters expressed through original a_{xx} and b_{xx} :

$$\begin{aligned} \hat{a}_{xx} &= a_{xx} \frac{\sin 4\Delta\varphi_s}{4\Delta\varphi_s} \\ \hat{b}_{xx} &= b_{xx} \frac{\sin 2\Delta\varphi_s}{2\Delta\varphi_s} \end{aligned} \quad (\text{E13})$$

And, finally:

$$\hat{r}_{xx} = r_{xx} \frac{\sin 4\Delta\varphi_s}{2\sin 2\Delta\varphi_s} \quad (\text{E14})$$

I.e. the observed \hat{r}_{xx} differs from the original r_{xx} by a factor which does not change its sign if $|\Delta\varphi_s| < 45^\circ$, so within this range our identification recipe stays valid.

F. STATISTICAL ERROR OF THE DISPERSION OF A SCALAR RANDOM FIELD

Let us take a homogeneous random field, which admits a spectral representation

$$s(\mathbf{R}) = \int e^{i\mathbf{K}\mathbf{R}} F(\mathbf{K}) \xi(\mathbf{K}) \sqrt{d\mathbf{K}}. \quad (\text{F15})$$

For its dispersion D_Ω , estimated over a limited area Ω , after some algebra we can write the following expression:

$$D_\Omega = \int F^2(\mathbf{K}) (1 - \Pi_\Omega^2(\mathbf{K})) d\mathbf{K} \quad (\text{F16})$$

where

$$\Pi_\Omega(\mathbf{K}) = \frac{1}{\Omega} \int_\Omega e^{i\mathbf{K}\mathbf{R}} d\mathbf{R} \quad (\text{F17})$$

Then the variance of D_Ω can be evaluated as follows:

$$\sigma_D^2 = 2 \int F^2(\mathbf{K}) d\mathbf{K} \int F^2(\mathbf{K}') d\mathbf{K}' \cdot (\Pi_\Omega(\mathbf{K} + \mathbf{K}') - \Pi_\Omega(\mathbf{K}) \Pi_\Omega(\mathbf{K}'))^2 \quad (\text{F18})$$

G. SPECTRAL REPRESENTATION OF A RANDOM FIELD

The following speculations are based on [Rozanov \(1990\)](#).

G.1. Scalar field

Let us write the correlation function of a homogeneous random field $\rho(\mathbf{r})$ as its spectral representation:

$$C(\mathbf{r}) \equiv \langle \rho^*(\mathbf{0}) \rho(\mathbf{r}) \rangle = \int e^{i\mathbf{k}\mathbf{r}} \mathcal{F}(d\mathbf{k}) = \int e^{i\mathbf{k}\mathbf{r}} F^2(\mathbf{k}) d\mathbf{k} \quad (\text{G19})$$

where F^2 is the correspondent power spectrum.

Every homogeneous field admits a spectral representation as follows:

$$\rho(\mathbf{r}) = \int e^{i\mathbf{k}\mathbf{r}} \Phi(d\mathbf{k}) \quad (\text{G20})$$

where $\Phi(\cdot)$ is a complex random measure in \mathbb{R}^3 , satisfying

$$\langle \Phi(A) \Phi^*(B) \rangle = \mathcal{F}(A \cap B) \quad (\text{G21})$$

Consequently, measure elements must conform the following symbolic rule:

$$\langle \Phi(d\mathbf{k}) \Phi^*(d\mathbf{k}') \rangle = \delta_{\mathbf{k}\mathbf{k}'} \mathcal{F}(d\mathbf{k}) = \delta_{\mathbf{k}\mathbf{k}'} F^2(\mathbf{k}) d\mathbf{k} \quad (\text{G22})$$

We would like to improve the notation Eq. [G20](#). It would be interesting to expose the internal structure of the spectral measure element. If we introduce the complex random field ξ as follows

$$\Phi(d\mathbf{k}) = F(\mathbf{k}) \xi(\mathbf{k}) \sqrt{d\mathbf{k}} \quad (\text{G23})$$

$$\langle \xi(\mathbf{k}) \xi^*(\mathbf{k}') \rangle = \delta_{\mathbf{k}\mathbf{k}'}, \quad (\text{G24})$$

we satisfy Eq. [G22](#). Then, Eq. [G20](#) can be rewritten in the following form:

$$\rho(\mathbf{r}) = \int e^{i\mathbf{k}\mathbf{r}} F(\mathbf{k}) \xi(\mathbf{k}) \sqrt{d\mathbf{k}} \quad (\text{G25})$$

where $\xi(\mathbf{k})$ conforms Eq. [G24](#) and $F(\mathbf{k})$ is a square root of the power spectrum. In addition, if $\rho \in \mathbb{R}$,

$$\xi(-\mathbf{k}) = \xi^*(\mathbf{k}). \quad (\text{G26})$$

G.2. Vector field

Let us generalize Eq. G25 for the case of a vector field.

Let us write the correlation function of a homogeneous vector random field $u_i(\mathbf{r})$ as its spectral representation:

$$C_{ij}(\mathbf{r}) \equiv \langle u_i^*(\mathbf{0})u_j(\mathbf{r}) \rangle = \int e^{i\mathbf{k}\mathbf{r}} \mathcal{F}_{ij}(d\mathbf{k}) = \int e^{i\mathbf{k}\mathbf{r}} F^2(\mathbf{k}) T_{ij}(\hat{\mathbf{k}}) d\mathbf{k} \quad (\text{G27})$$

where F^2 is the scalar part of the power spectrum, and T_{ij} is a spectral tensor, satisfying the equation

$$T_{ij}(\hat{\mathbf{k}}) = T_{il}(\hat{\mathbf{k}}) T_{jl}(\hat{\mathbf{k}}) \quad (\text{G28})$$

If also $T_{ij} = T_{ji}$, what is true in our cases, T is an orthogonal projector.

The spectral representation of the field itself can be written as follows:

$$u_i(\mathbf{r}) = \int e^{i\mathbf{k}\mathbf{r}} \Phi_i(d\mathbf{k}) \quad (\text{G29})$$

where $\Phi_i(\cdot)$ is a complex vector random measure in \mathbb{R}^3 , satisfying

$$\langle \Phi_i(A) \Phi_j^*(B) \rangle = \mathcal{F}_{ij}(A \cap B) \quad (\text{G30})$$

The correspondent symbolic rule can be written in the following form:

$$\langle \Phi_i(d\mathbf{k}) \Phi_j^*(d\mathbf{k}') \rangle = \delta_{\mathbf{k}\mathbf{k}'} \mathcal{F}_{ij}(d\mathbf{k}) = \delta_{\mathbf{k}\mathbf{k}'} F^2(\mathbf{k}) T_{ij}(\hat{\mathbf{k}}) d\mathbf{k} \quad (\text{G31})$$

Then the explicit form of the spectral measure element can be represented as follows:

$$\Phi_i(d\mathbf{k}) = F(\mathbf{k}) T_{ij}(\hat{\mathbf{k}}) \xi_j(\mathbf{k}) \sqrt{d\mathbf{k}}, \quad (\text{G32})$$

where the complex random field $\xi_i(\mathbf{k})$ must conform:

$$\langle \xi_i(\mathbf{k}) \xi_j^*(\mathbf{k}') \rangle = \delta_{ij} \delta_{\mathbf{k}\mathbf{k}'}. \quad (\text{G33})$$

This satisfies Eq. G31. Finally, Eq. G29 can be rewritten as follows:

$$u_i(\mathbf{r}) = \int e^{i\mathbf{k}\mathbf{r}} F(\mathbf{k}) T_{ij}(\hat{\mathbf{k}}) \xi_j(\mathbf{k}) \sqrt{d\mathbf{k}} \quad (\text{G34})$$

where $\xi_i(\mathbf{k})$ conforms Eq. G33, $F(\mathbf{k})$ is a square root of the scalar part of the power spectrum and the spectral tensor $T_{ij}(\hat{\mathbf{k}})$ conforms Eq. G28.

If the field is real, we also have

$$\xi_i(-\mathbf{k}) = \xi_i^*(\mathbf{k}). \quad (\text{G35})$$

REFERENCES

- | | |
|---|---|
| <p>Cho, J., & Lazarian, A. 2003, MNRAS, 345, 325</p> <p>Lazarian, A., & Pogosyan, D. 2012, ApJ, 747, 5</p> <p>Oppermann, N., Junklewitz, H., Greiner, M., et al. 2015, A&A, 575, A118</p> <p>Pandya, A., Zhang, Z., Chandra, M., & Gammie, C. F. 2016, ApJ, 822, 34</p> <p>Rozanov Yu. A., Stationary Random Processes, 1990, Nauka, Moscow</p> | <p>Erdélyi, R., Petrovay, K., Roberts, B., Aschwanden, M., Turbulence, Waves and Instabilities in the Solar Plasma: Proceedings of the NATO Advanced Research Workshop on Turbulence, Waves, and Instabilities in the Solar Plasma Lillafured, Hungary 16-20 September 2002</p> <p>Xiao, L., Han, J. L., Reich, W., et al. 2011, A&A, 529, A15</p> <p>Yan, H., & Lazarian, A. 2004, ApJ, 614, 757</p> <p>Wolleben, M., Landecker, T. L., Reich, W., & Wielebinski, R. 2006, A&A, 448, 411</p> |
|---|---|